

An Introduction to Ice-Penetrating Radar and UTIG's **pik1** Data Product

Laura Lindzey

December 9, 2015

1 Introduction

Radar has long been used to study Antarctica's ice sheets, which is possible because ice is almost transparent to electromagnetic energy at HF and VHF frequencies. The processed data images a 2D slice of the ice sheet, where many features are clearly visible. Figure 1 shows the air/ice interface, the ice/bed interface, crevasses at the base of the ice shelf, and layers within the grounded ice.

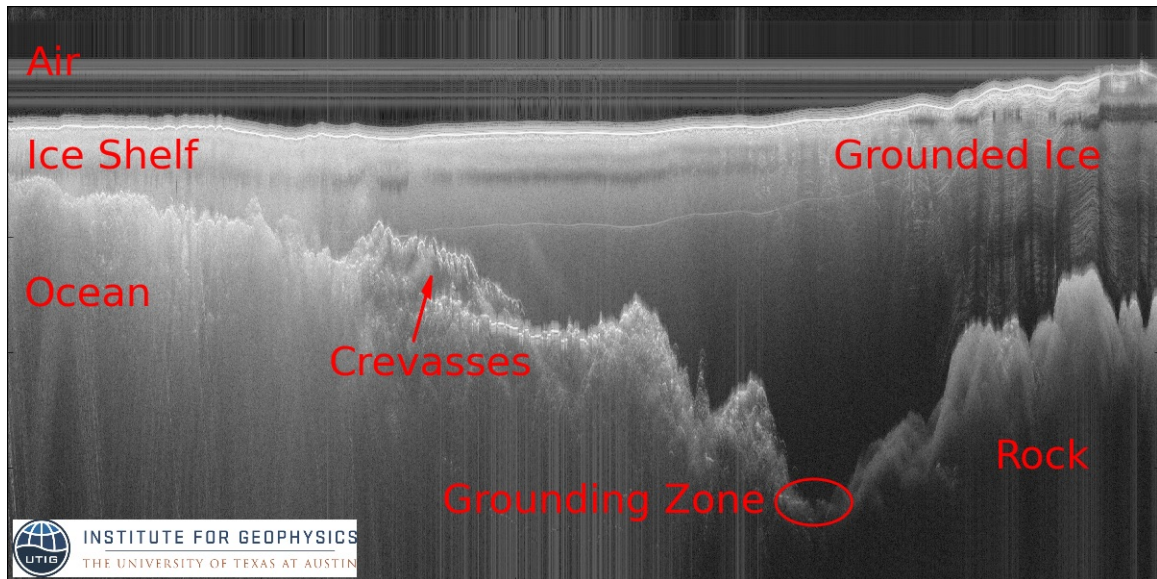


Figure 1: Example ice penetrating radar data, from a line over the Totten ice shelf (TOT/JKB2d/X16a). This transect's data will be used throughout the report. It is \sim 200km long, and the ice is \sim 2.8km deep at the grounding zone.

Applications for this data include: simply calculating ice thickness, as done by the Bedmap project [3]; tracing internal layers [8, 9] and correlating with ice cores to determine an age-depth relationship; identifying subglacial lakes [1] and inferring properties of the

subglacial water system [12–15]; using the returned pulse shape to infer surface roughness [6, 7]; and characterizing the location of complicated grounding zones [5].

In this project, I investigated the software processing required to generate the data product shown in Figure 1. While doing so, I figured out how to eliminate the vertical streaks in the image, which were an artifact introduced by a suboptimally implemented noise-reduction step. This report describes the hardware and software involved in collecting and processing the radar data and the analysis leading to my proposed algorithmic improvement and its implications.

2 Data Collection

Over the last few decades, Don Blankenship’s research group has collected airborne ice-penetrating data all over Antarctica. In order to collect this data, we mount antennas and recording equipment on a modified DC-3, as shown in Figure 3. Figure 2 shows everywhere that we have flown; the darker lines correspond to where the radar setup matches the system described in this report.

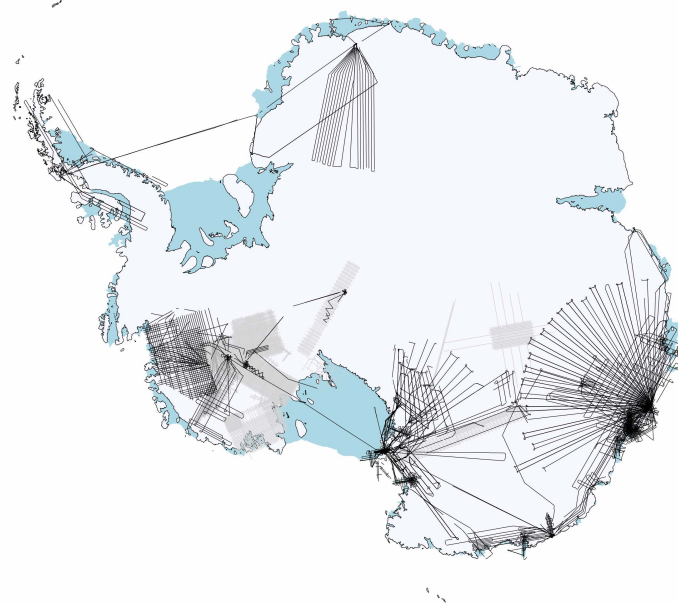


Figure 2: Map of Antarctica showing almost everywhere that UTIG has collected data. Black lines represent transects flown with the system described in this report.

As the plane flies, the radar transmits 6250 pulses every second. After each pulse, it listens for and records reflected energy; this returned signal is what you’re looking at in the radargram. Any change in the dielectric property of the medium will generate a reflection. The reflections ones are usually at the air/ice and ice/bed interface. When looking at a radargram like Figure 1, the x-axis is distance along the flight line, and the y-axis is height. In effect, we’re looking at a vertical slice of the ice sheet.

More precisely, both axes are in units of time - each column of the image corresponds to

the information received from a single pulse of the radar, and the rows are how much time has passed since the transmission, as recorded by the digitizer. We call the columns sweeps or traces, and the rows are samples. We also call the x-axis *slow time* since the pulses are at 6250Hz, while the y-axis is *fast time* because the digitizer samples at 50MHz.

2.1 Beam Pattern



Figure 3: JKB, one of the DC-3s that has been modified to carry our instrument suite. Note the antennas under the wings. (Photo: Chad Greene)

Two dipole antennas, separated by 18.95m (Figure 3) generate the beam pattern shown in Figure 4. They are mounted a quarter wavelength under the wings, and both antennas are used for both transmit and receive.

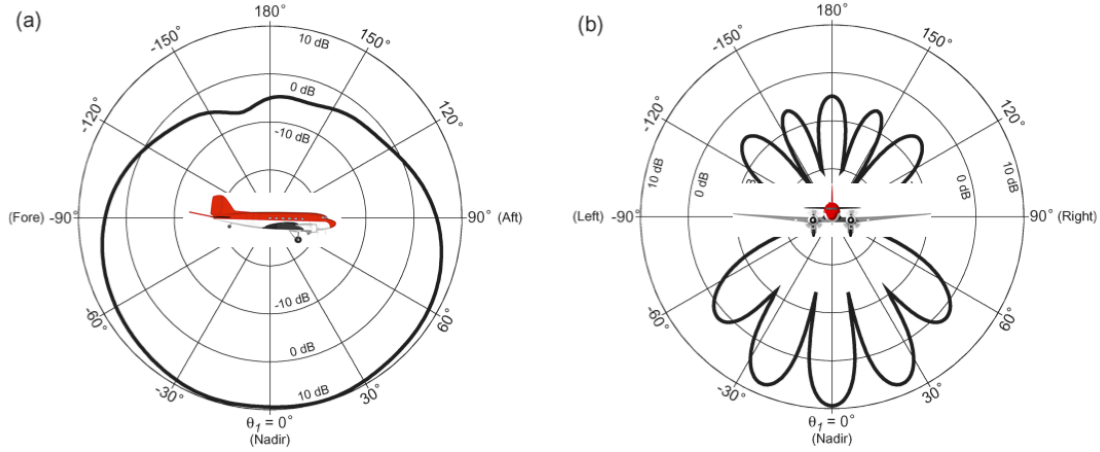


Figure 4: (Left) The along-track beam pattern that results from our antenna placement. (Right) The across-track beam pattern. (From [10])

The broad beam pattern and strong side lobes mean that in addition to echoes directly below the airplane, we detect significant off-nadir energy, which adds clutter to the radargram and lowers the spatial resolution. Many of the processing steps are aimed at reducing these effects. It is easier to improve along-track resolution because we have many overlapping observations. Clutter from the sides is more difficult to reduce.

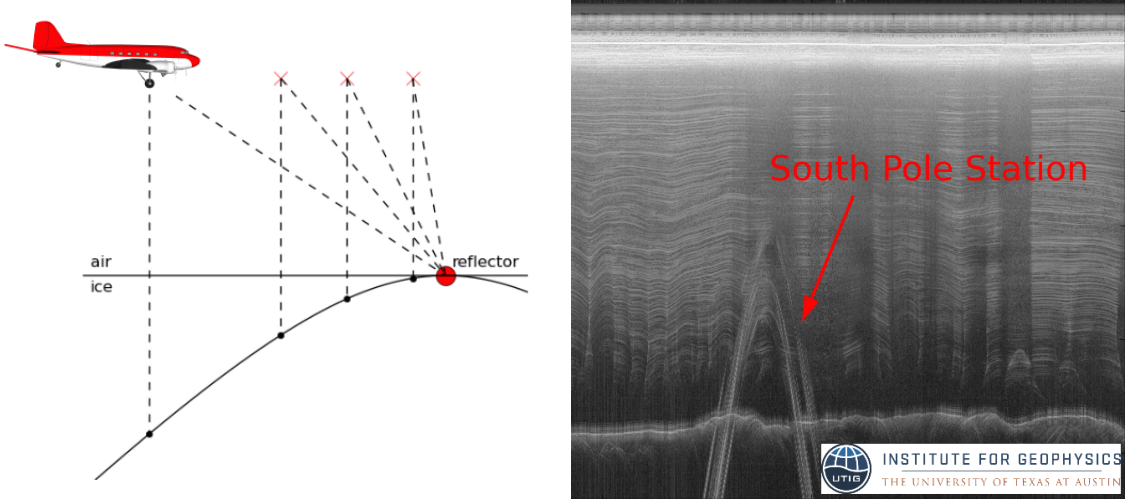
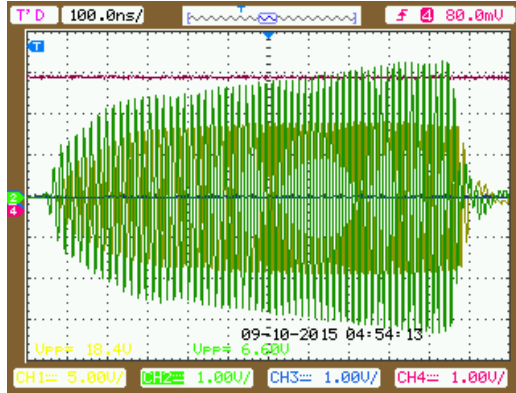


Figure 5: (Left) geometry for strong point reflector to show up in the data as a hyperbola. (Right) Example hyperbola from South Pole Station

2.2 Details of Radar Electronics

The transmitted energy is a $1\mu\text{s}$ wide chirped pulse, with a 60MHz center frequency and 15MHz bandwidth. It is generated digitally by a PXI controller with samples at 200MHz, and fed into an 8kW Tomco amplifier. Figure 6 shows the resulting transmitted pulse shape. The pulse repetition frequency of the current system is 6250Hz, which means if the airplane is flying at the nominal 90m/s, it is taking a measurement about every 1.5cm along track.



*Illustration 1: Tomco VT8C 11068,
Ch1 (yellow) is 40 dB attenuated pulse*

Figure 6: Oscilloscope trace of attenuated amplifier output. (Credit: Gregory Ng, EC15036)

As discussed in Section 2.1, we use both antennas for both transmit and receive. This is enabled by routing the amplifier's output signal through a transmit/receive (T/R) switch, a splitter/combiner, and out to the antennas.

For the system described in this report, the returned signal was downconverted before digitization. Recent improvements in digitizers has enabled us to do bandpass sampling without the downconversion. The downconversion is performed by mixing the signal with a 70MHz local oscillator, then low pass filtering the output.

The PXI also generates a blanking signal that brackets the outgoing chirp. The receive electronics use this to determine whether to digitize the output of the T/R switches or the attenuated reference chirp from the amplifiers.

In order to achieve a 130dB dynamic range with only 14 digitizer bits, the returned signal is split into high and low gain channels. Each channel is recorded separately; the low gain one does not saturate at the surface, so it is used for any near-surface applications, while the high gain one is used for detecting deeper layers and faint bed returns.

Before writing the data to disk, 32 consecutive traces are summed. This is required to maintain a feasible disk write rate, and the justification is the same as for software stacking in Section 3.4. The 3 least significant bits are dropped, resulting in 2 bytes per sample.

The receiver electronics saturate at 1V peak-to-peak and write 16bits to disk (14-bit digitizer, with 32x hardware stacking and dropping the 3 least significant bits before writing to disk). In order to convert from counts to power or voltage we use:

$$\begin{aligned} 2^{16} \text{ counts} &= 1.0V_{pp} \\ V_{rms} &= \frac{1}{2\sqrt{2}}V_{pp} \\ 0\text{dBm} &= 10\log_{10} 1mW \\ \text{Power (W)} &= \frac{V_{rms}^2}{Z} \end{aligned}$$

For a system with 50Ω impedance, if a signal is C counts peak-to-peak in the raw data it is $10\log_{10} \left(1000 \frac{\left(\frac{1}{2\sqrt{2}} 2^{16} \right)^2}{50\Omega} \right)$ dBm.

2.3 Coherence

In the context of radar, we use *coherent* to mean a number of slightly different things:

1. To describe a radar system that is able to capture phase information about the signal. This requires sending out pulses of energy where the phase is always consistent with respect to the start of the pulse. For example, if you generated the output signal using an unsynchronized oscillator and a blanking signal, you'd have an incoherent radar. It also requires sampling the returned signal at a high enough frequency and good enough precision to recover the phase information.
2. To describe an interface that reflects energy while preserving phase. A uniform mirror-like flat surface will be coherent. If a surface is rough, reflections from different points will vary in phase, and the aggregate signal will be incoherent.
3. To describe whether the processing applied to the data has preserved phase information. Early steps in our processing pipeline retain phase information, and later ones operate only on amplitudes. Reducing different types of noise require coherent or incoherent techniques. The ordering is important since once you've discarded phase information you can't get it back.

The old radar system (grey lines in Figure 2) was incoherent. Adding the ability to recover the signal’s phase allows us to use a chirped signal for pulse compression and perform focusing.

3 The pik1 Data Product

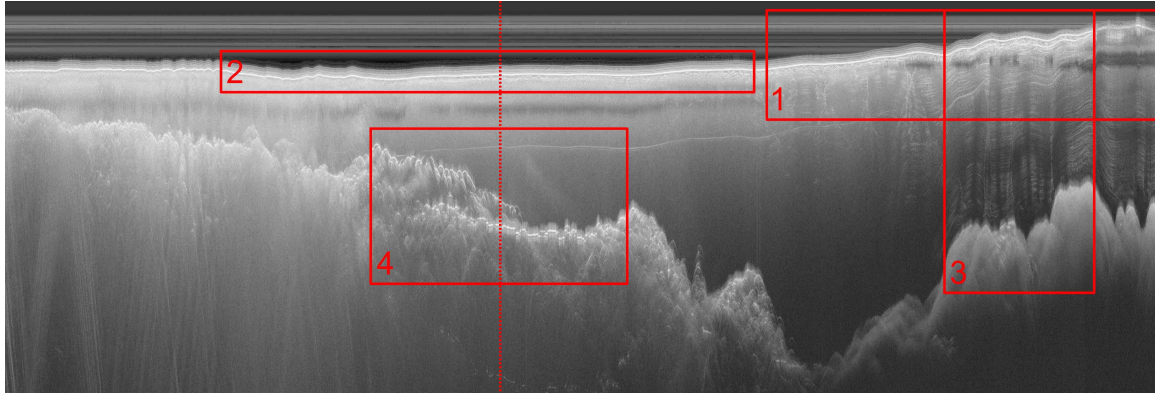


Figure 7: Example **pik1** data product. The numbered boxes and vertical line show regions that are used to highlight the effects of different processing steps.

pik1 is the simplest and least-processor-intensive radar data product that our group produces. It is primarily meant as a field quality control product, suitable for analyzing after each flight in order to determine whether we successfully gathered the data required to answer our scientific questions. An example can be seen in Figure 7. It is also used for preliminary surface and bed labeling that leads to ice thickness estimates. Our primary products meant for scientific analysis are the focused radargrams (Section 6.2).

This rest of this section describes the processing steps involved in generating the **pik1** data product.

3.1 Pre-Processing Raw Data

As we transmit the signal, it also interacts with the airplane, creating a very loud noise signal that we call the *main bang*. This is partially masked in hardware in order to protect the digitizers and allow us to record an unsaturated reference chirp. However, the noise continues well past the end of the hardware blanking.

Received wisdom is that we need to blank the first ~ 200 samples of the raw data as the first processing step in order to mask the main bang. Figure 8 shows the relative timings of the transmitted chirp, main bang, hardware and software blanking. The hardware blanking is used to switch the receiver’s input from the T/R switch to an attenuated version of the transmitted pulse fed in from the amplifier’s output.

The additional software blanking step doesn’t make sense to me: it was always a question of how much to blank without risking cutting off part of the surface return; the samples that are zeroed mostly overlap with the blanking that has already been performed in hardware;

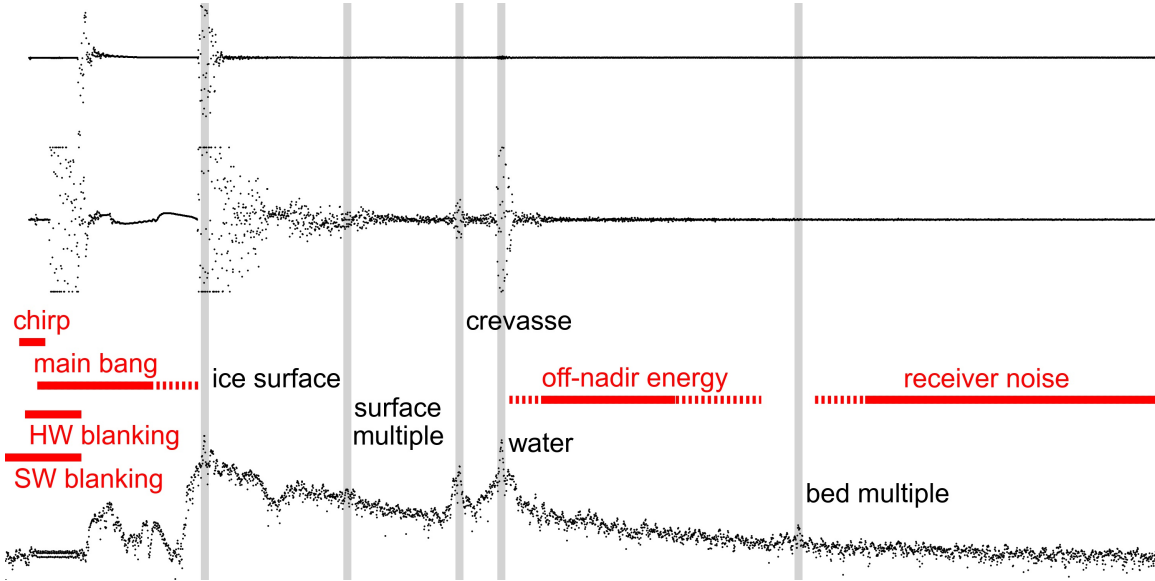


Figure 8: A single raw trace as recorded by the digitizers (top - low gain, center - high gain), and the resulting **textbf{pik1}** product for high gain channel. (bottom). Trace location is shown as the dotted line in Figure 7.

and I haven't found a transect where leaving this step out affects the appearance of the **pik1** product.

While the low gain channel in Figure 8 behaves as expected, the high gain channel appears to have a significant DC offset. Looking at Figure 9, we can see that the odd dark regions under the surface only appear in the high gain data, and only where we are flying near to the surface, which suggests that these artifacts might be related.

The consistency of the pattern above the surface in the raw data and dechirped data suggests that it might be possible to subtract this signal out. Characterizing the noise properly would be most straightforward if I could find a transect that was flown at a very high elevation. However, it is not clear whether there is any scientific justification to doing this characterization: if it is only a near-surface effect, and only appears in the high gain data, then it's not a problem, since we can use the low gain data. However, looking at the raw data in Figure 10, it appears that the oscillations continue beyond the near surface. Thus, they might be contributing to an increased noise floor even if we can't see them in the **pik1** product.

3.2 Pulse Compression

It is possible to see a surface and bed in the raw amplitudes recorded by the digitizer, but this image does not have anywhere near the resolution that we would hope for. Since we transmit a chirped signal, the first step in processing is to perform *pulse compression* - also referred to as *range compression* or *dechirping*. This simply requires convolving a reference chirp with each received trace, and it immediately improves the appearance of the surface and bed, as can be seen in Figure 10. In practice, this is done more efficiently using the convolution

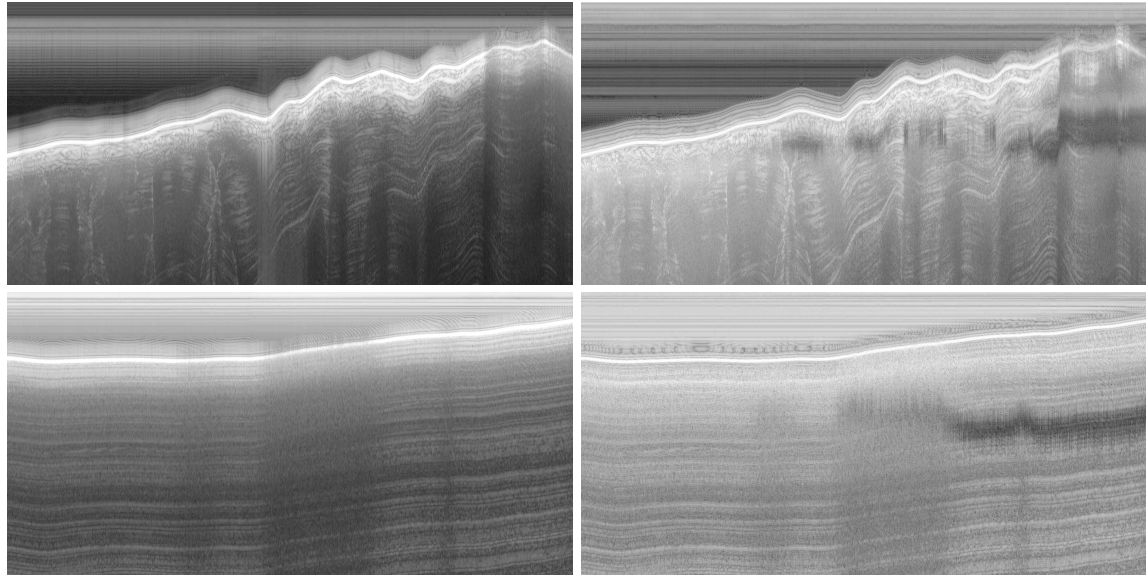


Figure 9: Low gain (left) and high gain (right) radargrams from when the airplane was flying less than $\sim 600\text{m}$ from the surface. Transects are TOT/JKB2d/X16a (top) and VCD/JKB2g/DVD01a (bottom). The TOT data is from box #1 in Figure 7.

property of the Fourier Transform: $\text{chirp} * \text{trace} = iFFT(FFT(\text{trace}) \cdot FFT(\text{chirp}))$

Examination of Figure 8 shows that the first sample of the raw data has to be offset by 66 traces in order for it to line up with the final **pik1** data product. This is due to the fact that the reference chirp used in the pulse compression does not start at the first sample. Thus, the peak energy when convolving the reference chirp with a theoretical chirp that starts at sample 0 occurs at a later sample.

Additionally, the reference chirp must be flipped to sweep from high to low frequency. This is because the down conversion changes the signal to 70MHz - chirp, and for a $52.5 \rightarrow 67.5\text{MHz}$ chirp, this results in a $17.5 \rightarrow 2.5\text{MHz}$ signal.

3.3 Filtering

As part of the pulse compression step, we apply a window function (Figure 11) to the trace's FFT. This has the effect of further sharpening interfaces (Figure 12).

3.4 Coherent Stacking

Since the data is recorded at about 195Hz (the radar pulse repetition frequency is 6250Hz; we stack 32x in hardware) and the plane flies at about 90m/s, we have traces spaced about every 50cm. This is excessive along track sampling for any human-viewable data product. For comparison, our across track 3dB beam width is 12° and our along track beam width is 152° [10]. So, flying at an altitude of 600m, our effective pulse shape is $126\text{m} \times 4.8\text{km}$. The effective footprint is significantly smaller than this, since it is *pulse limited* based the maximum off-nadir angle before returned energy begins to destructively interfere.

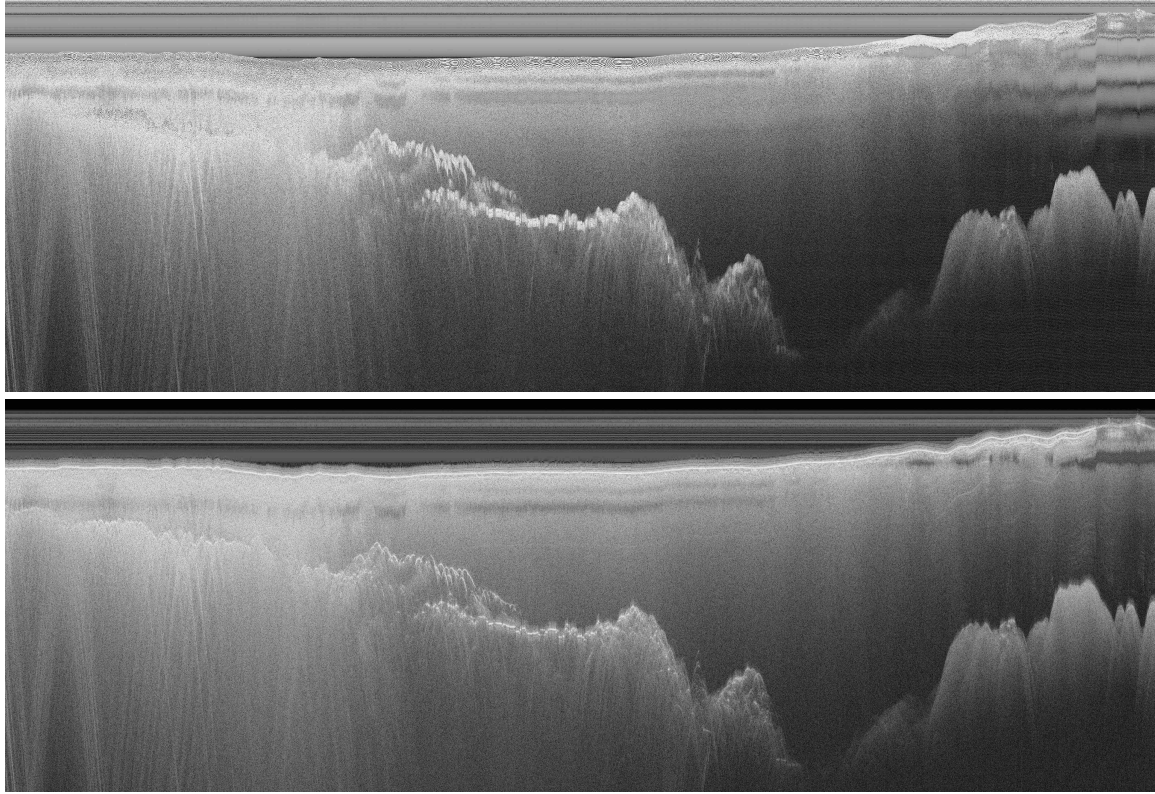


Figure 10: Pulse compression sharpens interfaces. (Top) Magnitude of raw radar returns. (Bottom) After dechirping.

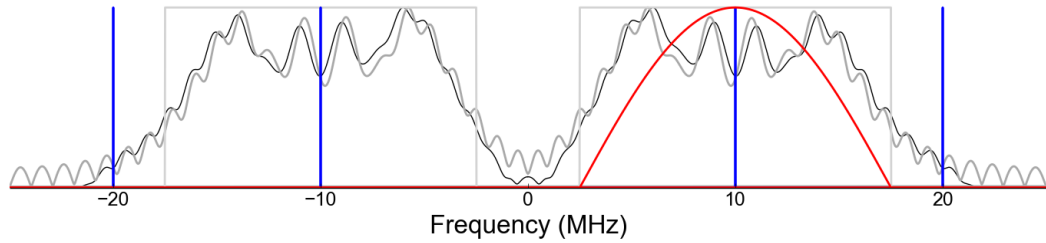


Figure 11: Frequency space representation of the filter (red) and other signals in the system. FFT of Local Oscillator (70MHz) and LO's first harmonic (140MHz) are in blue. Ideal chirp frequency spectrum is light grey, 3200-bin FFT of 50MHz sampled ideal chirp in dark grey, and FFT of the chirp used in processing is black.

We perform additional stacking in software; this has two primary benefits.

First, it improves our signal-to-noise ratio. Since the footprints of successive pulses almost entirely overlap, we treat them as repeat measurements of the same scene, for which we'd expect the SNR to improve with \sqrt{n} . The maximum effective stacking depth is determined by how many consecutive returns can be added before the first and last begin to

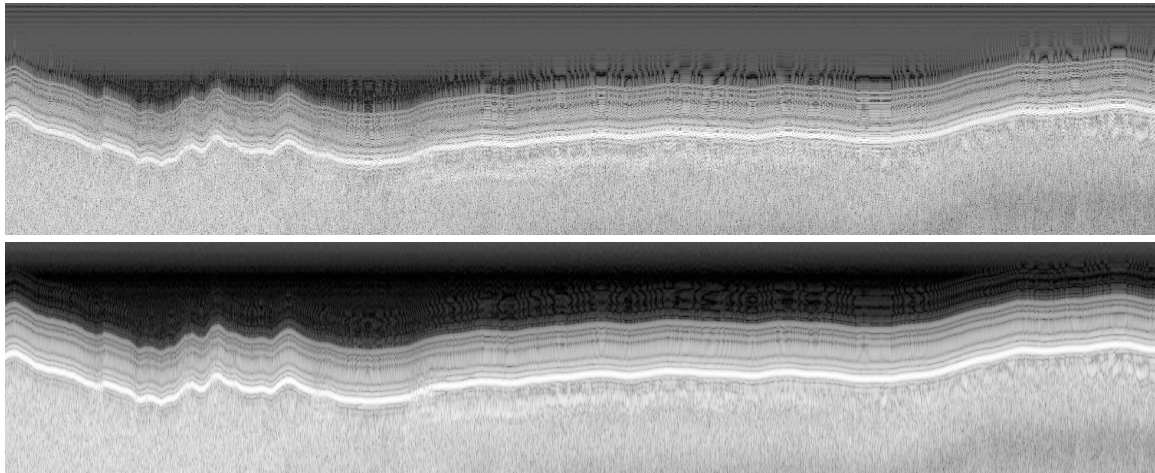


Figure 12: Zooming in on the surface shows the effect of filtering. This region is box #2 in Figure 7. (Top) Dechirped. (Bottom) Dechirped and filtered.

destructively interfere. (In practice, we don't want them to differ by more than $\frac{\lambda}{4}$.) This will be governed by either the *pulse limited footprint* or how quickly the terrain changes. In practice, we have found that a depth of 10 works well at this stage.

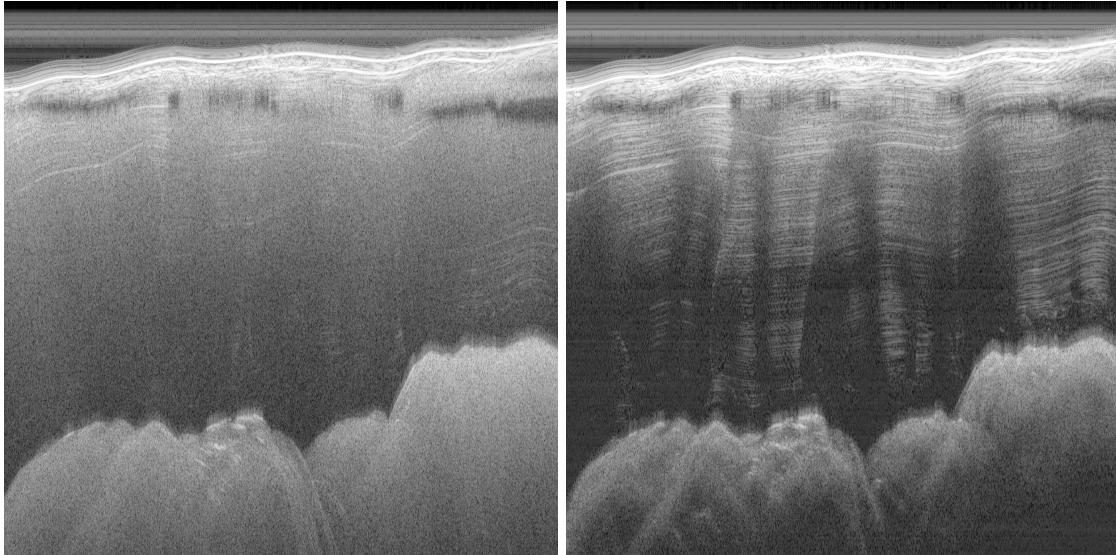


Figure 13: Coherent stacking improves the SNR, revealing layers. Improved horizontal resolution can also be seen at the bed. This region is box #3 in Figure 7. (Left) Dechirped (Right) Dechirped and coherently stacked 50x.

Second, it increases our along-track resolution. This technique is also referred to as *unfocused Synthetic Aperture Radar* or *coherent integration* [11]. The intuitive explanation of unfocused SAR is that for a single pulse, you have energy from the entire footprint given by the beam pattern. If you add multiple consecutive pulses, the energy from their

overlapping portions will constructively interfere while the energy from the non-overlapping borders will destructively interfere. Thus, the more pulses you add, the smaller your effective footprint.

3.5 Incoherent Stacking

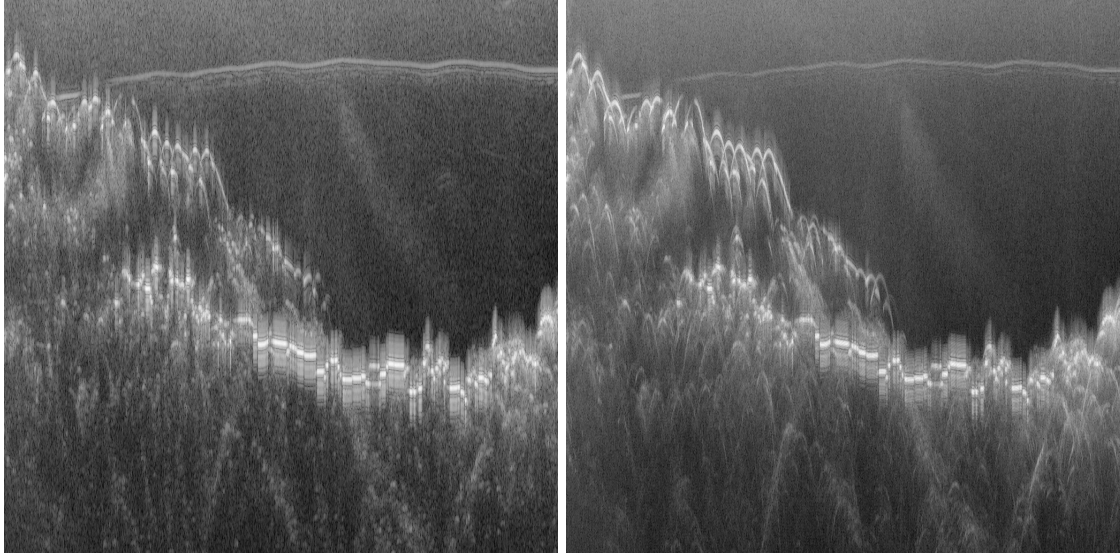


Figure 14: Incoherent stacking alleviates speckle. This region is box #4 in Figure 7. (Left) coherently stacked 50x (Right) coherently stacked 10x, incoherently stacked 5x.

While coherently stacking the returned traces is fantastic for improving the signal to noise ratio, it is unable to address some types of noise. *Speckle* is caused by constructive and destructive interference of the waveforms. It is the same effect as you'd see looking at a laser pointer's dot. Additional coherent summation simply moves the peaks and nulls around; it is unable to eliminate them. Reducing noise due to speckle requires summing the magnitudes of the traces rather than the full waveform. We call this *incoherent stacking*, and the results can be seen in Figure 14.

3.6 Implementation

Data processing pipelines that require streaming data (rather than operating on the entire data set at once) can be implemented elegantly by chaining generators in python. At the highest level, the **pik1** algorithm looks like:

```
# Reads from disk and yields one trace at a time
traces = read_raw_data(...)

# Gathers depth traces and yields their sum
coherent_stacks = coh_stack_gen(traces, depth, ...)

# Performs dechirping and filtering on single input trace, yields the result
dechirped_traces = dechirp_gen(coherent_stacks, ...)
```

```

# Gathers inco_depth traces and yields the sum of their magnitudes
inco_traces = inco_stack_gen(dechirped_traces, inco_depth, ...)
# Reads one trace at a time and writes to disk
write_data(inco_traces, ...)

```

Since addition and convolution commute, coherent stacking and dechirping can be performed in either order. For performance reasons, we stack first. Filtering and the local oscillator correction both happen in frequency space, which means that they are performed at the same time as dechirping. The TOT/JKB2d/X16a transect used throughout this report represents just under an hour of radar data, has a raw file size of 5.8G. Generating the corresponding 111M **pik1** product required under a minute on my laptop.

4 Local Oscillator Noise

Some energy from the 70MHz local oscillator signal used in the frequency down conversion leaks through the low pass filter. When there is very little energy coming back from the antennas, this signal can become significant. Figure 15 shows horizontal stripes that result from this signal. (Of course, the stripes that are visible when the full radargram is shrunk down for plotting are aliased from the actual frequency.)

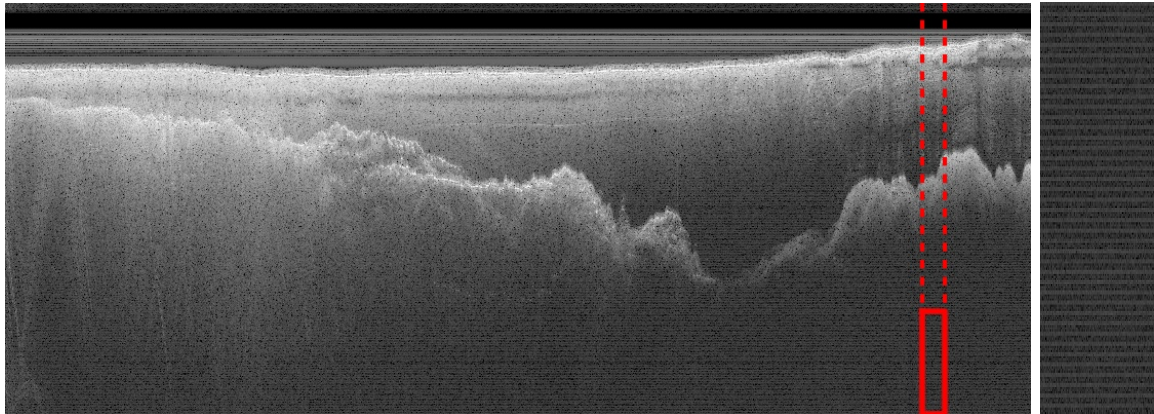


Figure 15: (Left) Data product with horizontal stripes due to aliased signal leakage from the 70MHz local oscillator. Rectangle shows automatically-selected quiet region for LO noise characterization. (Right) zoomed in on last 200 samples.

In addition to being a visual distraction, the energy leakage that causes these horizontal stripes also contributes to a higher noise floor. Since the noise floor is a key performance metric of our system, several people had previously tried to come up with a processing improvement that would reject this LO noise.

When I started looking at **pik1**, the existing way of dealing with this noise was to modify the FFT of the returned trace by replacing the values of the 4 bins contaminated by the LO noise with the average of their neighbors. This seemed to work (it fixed the noise floor issue) but whenever there were bright bed reflections it introduced the vertical streak artifacts that are apparent in Figure 1.

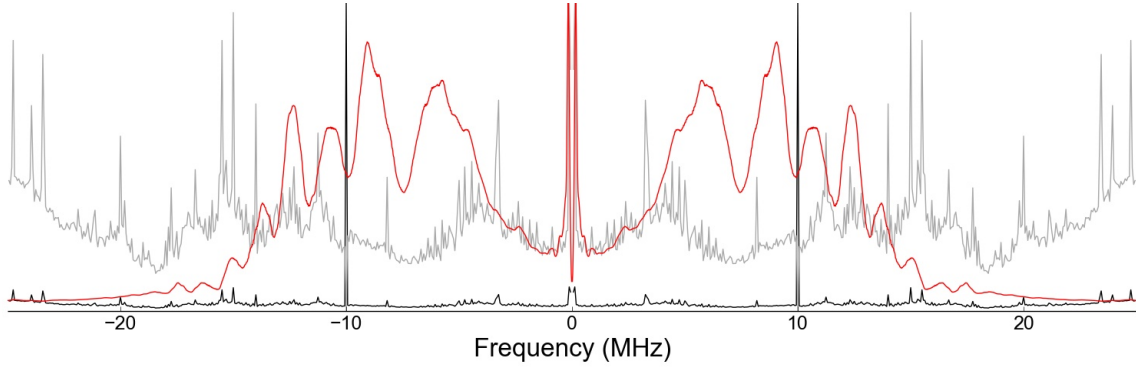


Figure 16: Frequency analysis TOT/JKB2d/X16a’s selected quiet region as shown in Figure 15. Red is average of the FFT of full traces in the region between the dashed lines. Black is (normalized) FFT of the selected region within the box, with the value at 0MHz removed. Grey is (normalized) FFT of the selected region with the components at 0, 10 and -10MHz removed. Vertical scale is linear.

An obvious approach to removing this noise would be to find a region of the transect with minimal echo signal energy and characterize its frequency content. Supposedly a similar approach had been tried before; I do not know why they were unable to get it to work. There are a few subtleties to this approach.

First, looking at Figure 16, it is clear that the LO’s contribution cannot be isolated if we take the FFT of full traces (red). However, but if we limit ourselves to the last 800 samples, we obtain clear peaks at -10 and 10Mhz (black). After removing those peaks, there are no additional dominant noise frequencies (grey). Due to the filtering discussed in Section 3.3, only the peak at 10MHz is relevant. Thus, to get rid of the LO noise we can simply subtract off the magnitude and phase of the 10MHz bin from the data’s FFT.

The quiet region must be chosen such that the phases will match up between region and the full transect. Using traces 2400-3200 has the nice property that the phase of a 10MHz signal will be the same as for traces 0-3200. Using a different subset of traces would require adjusting the computed noise phase.

Converting the noise amplitude and phase determined from a 800-point FFT to values that can be used with the 3200-point FFT given by: $FFT_{3200}[4k] = 4FFT_{800}[k]$, where the factor of 4 is from 3200/800.

Finally, care must be taken to properly scale the correction based on how many traces were used to calculate it and how many traces have been stacked before it will be applied.

The phases vary between transects, and we have thousands of transects, so implementation of this correction will be made significantly easier if we automatically choose a quiet region. This automatic selection has been implemented and shown to work on a few transects. QC images such as Figure 15 can be generated showing which regions were selected. In the case of a transect that consists entirely of deep ice where a sufficiently quiet region cannot be found, I can think of two alternatives. The first alternative would be to use fewer than 800 samples; the only real constraints are that more samples are better, the number of samples used needs to evenly divide 3200 (for cleanly converting between FFTs

with different numbers of bins) and needs to be a multiple of 5. It might also be possible to extend into using the last 237 traces that are normally discarded in order to keep our current system's data consistent with previous data.

5 Discussion

The local oscillator correction does not only apply to the **pik1** data product described in Section 3: it impacts every data product that we generate from the affected seasons' data. Improved digitizer performance has allowed the newest version of the receiver electronics to perform bandpass sampling and eliminate the LO, so this will not be needed for last season (dark grey lines in Figure 2's map) and any future seasons.

Figure 17 shows the improvement in **pik1** for 4 problematic transects. From top to bottom, they are: TOT/JKB2d/X14d (2010/2011), TOT/JKB2d/X16a (2010/2011), THW/SJB2/DRP02a (2004/2005), VCD/JKB2g/DVD01a (2011/2012). The elimination of the vertical stripes has made it possible to identify what we call *basal multiples* in some ice shelves. These are echoes corresponding to the radar energy that reflects from the ice/air interface and makes two round trips through the ice shelf.

Figure 18 shows some of the basal multiples that were not apparent in the old **pik1** product. These are valuable for a number of reasons. First, interpreting radar data over ice shelves is very challenging. Due to the presence of basal crevasses, it can be hard to tell which echo actually corresponds to the ice-water interface and leads to an accurate ice thickness calculation. If the multiples are present, it is almost certain that they correspond to a reflection off basal interface and not a crevasse. Second, they can be used to improve inferences about the melt/freeze distribution of the ice shelf.

The radar equation gives the received power (P_r) as a function of radar system parameters and the properties of the media that the signal has traveled through:

$$P_r = P_t \left(\frac{\lambda}{4\pi} \right)^2 \frac{G_a^2 T^2 L_i^2 L_s G_p}{[2(h + z/n_2)]^2} R \quad (1)$$

The radar instrument is characterized by its transmitted power P_t , center frequency wavelength in air λ , antenna gain G_a and system losses L_s . The spreading loss $[2(h + z/n_2)]^2$ depends on the ice thickness z , airplane height above the ice surface h and the ice's index of refraction is $n_2 = 1.78$. T is the one-way transmission loss for the air/ice interface.

The radar signal attenuates due to dielectric loss as it passes through the ice, represented by L_i , and the basal reflection coefficient R varies depending on the characteristics of the bed. Ice loss is predominantly controlled by temperature, while the reflection coefficient depends on both basal roughness (scattering losses can be ~ 10 dB) and whether there is water at the bed, which creates a much stronger reflection.

Usually, a dielectric loss model is assumed and the radar equation is used to solve for R in an attempt to identify water at the bed. However, if you know what the basal properties are, it can also be used to invert for L_i and thus ice temperature. In the context of an ice shelf, this is reasonable - we know that there is water at the base, and there are specular regions where we can assume minimal scattering.

Having the multiples is particularly valuable because if we have P_r from the primary ice/water echo and the multiple, all of the terms other than L_i and R cancel out, reducing

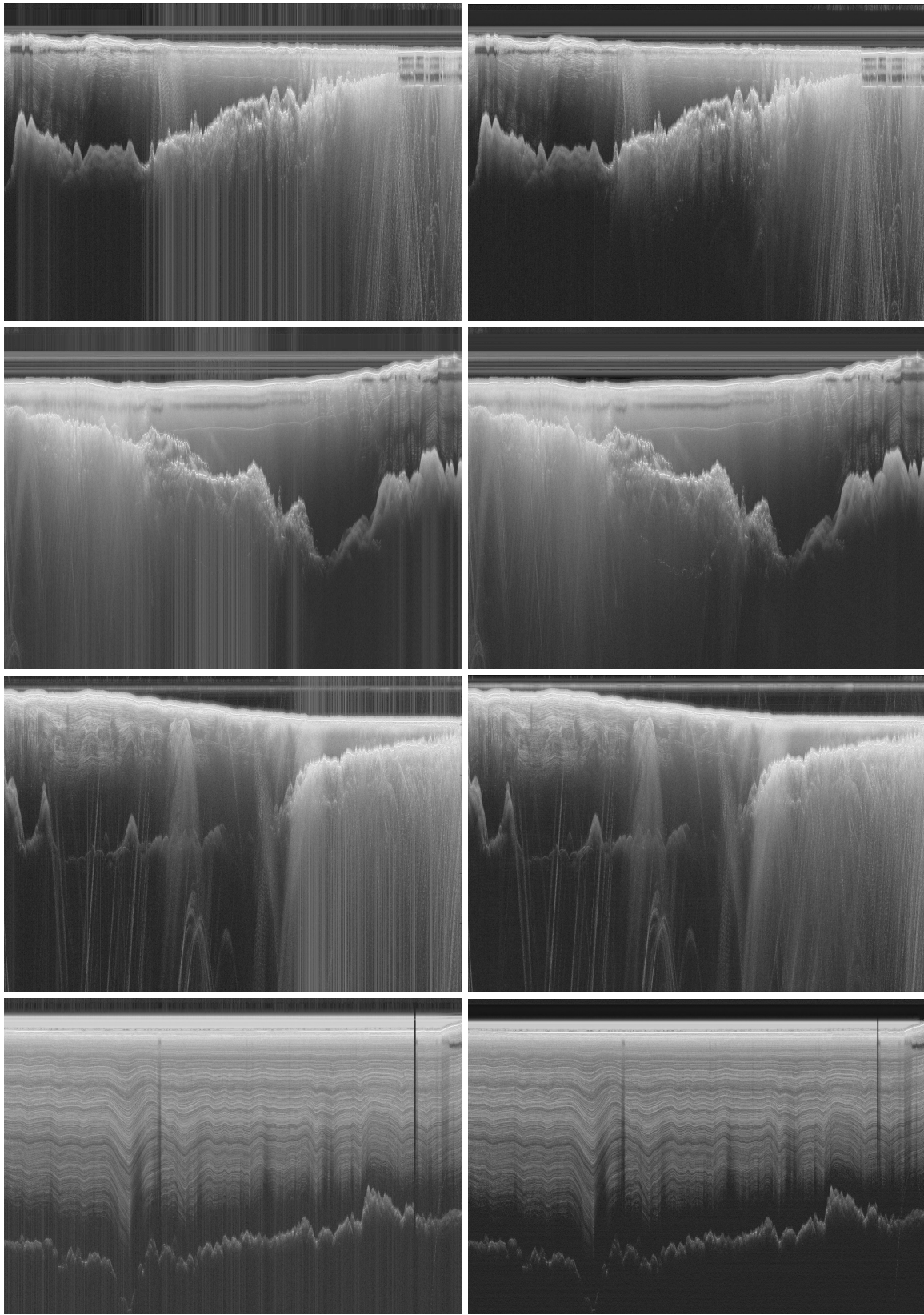


Figure 17: Demonstration of **pik1** improvements showing old (left column) and new (right column) approaches to LO correction for transects significantly affected by LO noise.

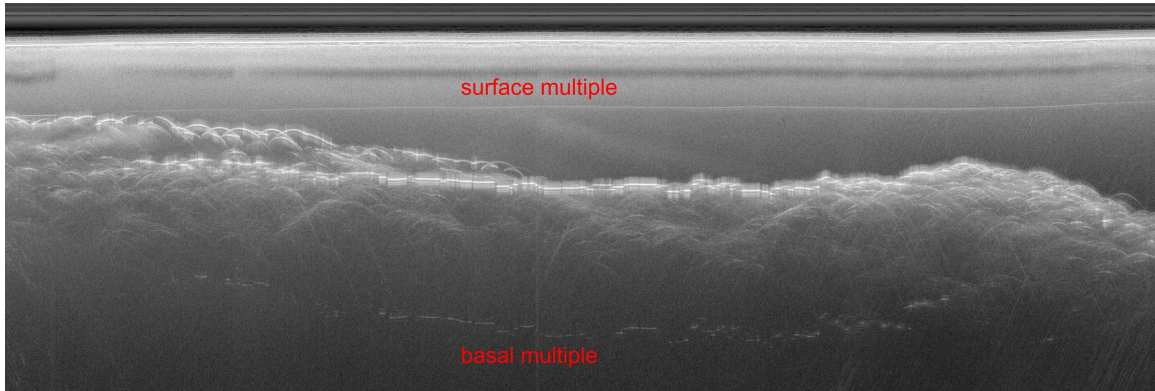


Figure 18: Image showing surface (two round trips between plane and ice surface) and basal (two round trips between air/ice and ice/water interfaces) multiples under an ice shelf.

the uncertainty in the resulting calculations. The temperature of an ice shelf is interesting because it will give us information about the melt and freeze distribution: melt will locally depress the column-average temperature, leading to higher reflection coefficients. I hope to use this technique to test hypotheses about how channels in the shelf affect melting.

6 Future Work

6.1 Raw Radar Data and **pik1**

While I have spent significant time looking into the **pik1** data product, I still have some questions that I'd like to investigate further:

- Why do we use the reference chirp that we use, and where did it come from? It doesn't match the theoretical chirp or the reference recorded from the amplifier's output. The goal is to match the output pulse shape as transmitted from the antennas, but we are not able to directly measure that. In the past, Duncan Young has attempted to use the received signal from sea water (since it is a fantastic reflector), but he says that it wound up being a good sea water detector but not good for other applications.
- I'd like to dig into the high gain channel DC noise as discussed in Section 3.1.
- Section 3.3 visualized the effects of filtering as currently implemented, but I still don't properly understand why that's the right thing to do in this application.
- I would like to perform a quantitative analysis of which stacking depth is ideal, since at this point all I have is the qualitative fact that the **pik1** product is an improvement over no stacking. This is the investigation that's least likely to make it into my group's released data products due to an issue with data consistency. We could change the balance between incoherent and coherent, but all of our final data products have the same horizontal resolution, corresponding to a total stack depth of 50x.

6.2 Focusing

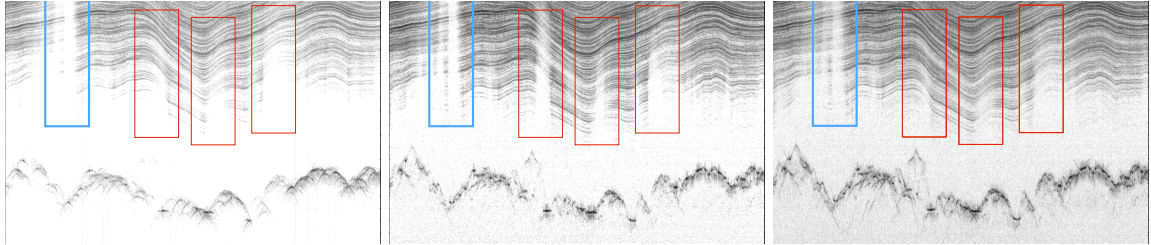


Figure 19: Image showing **pik1**, **foc1**, **foc2** for the same region of a transect. Note the improved layer resolution. (Credit: Duncan Young)

Our group’s main radar product is *focused* radar data. Focusing uses the fact that as the plane flies a point reflector will show up as a hyperbola in order to “move” the energy that creates the hyperbola tails shown in Figure 5 back to the point that generated it. The resulting image is often much less cluttered, allowing better identification of the bed reflection and internal layers. It does this by convolving a reference function with the raw radargram. This is a very computationally expensive operation because that reference function is a 2D array that must be computed for every different combination of point depths below the surface and plane height above the ice.

We generate two different focused products, **foc1** and **foc2**, corresponding to different widths of the reference function. Comparing the results of different focusing lengths is used in generating estimates of specularity [12].

On ice-shelves, it is known that focusing doesn’t work very well. This is because the algorithm assumes that all reflectors are point sources generating hyperbolas. However, there are often basal crevasses, which are fantastic corner reflectors (which send the returned energy back on a vector parallel to the incident vector.) If the crevasse is aligned obliquely to the flight path, the hyperbola will have a different curvature than you’d expect for one generated by a point source at the hyperbola’s apex.

I am interested in whether we can use this difference in hyperbola geometry to determine the angle that the crevasses are aligned to the flight path. Ideally, this would be done automatically; I wonder whether it is possible to calculate a set of focused radargrams assuming different crevasse orientations, and use the relative intensities in each radargram to determine the most likely orientation. While I understand the intuition of focusing, I have not yet had the chance to look into any implementation details, so I don’t have a very clear idea of what is computationally feasible. The alternative is to hand-label crevasse tails and fit a curve to them, but this requires a lot of human effort and would only work for very well defined hyperbola tails, limiting where it is applicable.

6.3 Multi-Antenna Processing

An emerging area of research is using multiple receive antennas to enable beam forming. While the sparse nature of the flight lines and expense of collecting data in Antarctica mean that the maps will still be interpolated from 1-D flight lines, it is important to be able to

determine which direction energy returned from in order to reject clutter when attempting to identify the ice/bed boundary. Recall from Section 2.1 that the radar's beam pattern has relatively strong side lobes at $\sim 23^\circ$ off-nadir. This means that we will often receive echoes that appear to be a bed reflection but are actually from off to the side. The radargrams in Figures 21 & 20 illustrate this problem.

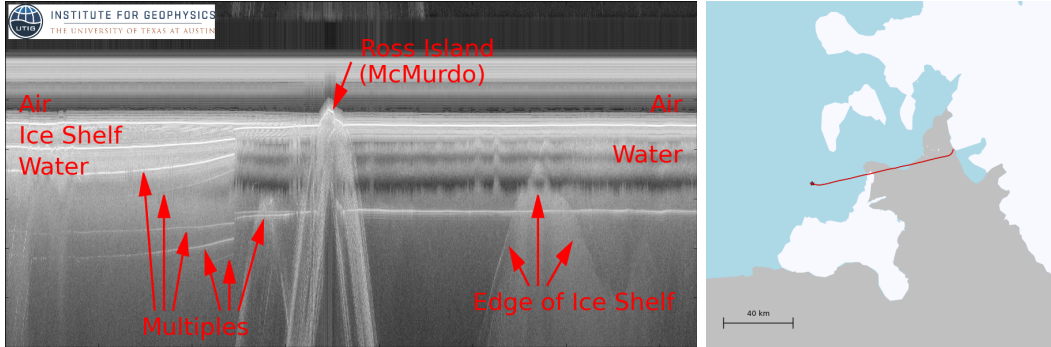


Figure 20: (Left) Radargram taken along the edge of the ice shelf where the echo from the side of the shelf could be mistaken for a bed reflection if the interpreter wasn't careful. (Right) Flight path for the radargram. Ice shelves are blue, open water is grey. Note how the geometry matches with the radargram.

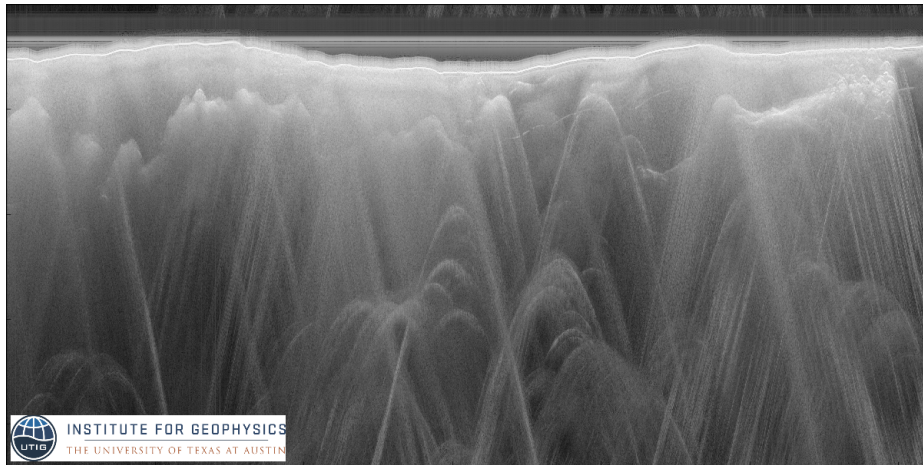


Figure 21: Radar data from flying down a valley. There is significant clutter from the mountains to either side.

Last season, UTIG fielded a system called MARFA that independently records from each of two antennas. This means that the phase difference between the two antennas can be used to determine whether an echo originates from directly below the airplane or from off to the side. This has been demonstrated to successfully discriminate surface clutter [2]. Unfortunately, this is only two antennas, and they have a wide enough baseline that phase cycles relatively rapidly. We are working on how to visualize the phase information, and how to extend this result to basal clutter.

CReSIS has been experimenting with recording from multiple antennas oriented across track with their MCoRDS radar instrument. They have also succeeded at clutter discrimination [4], and have managed 3D swath surface and bed reconstructions [16].

Acknowledgements

I owe a huge thanks to my colleagues at UTIG for our discussions about this radar system. Duncan Young, Gregory Ng and Scott Kempf fielded many questions about the local oscillator noise, previous attempts to address it, and how to validate my approach. Duncan Young, Gregory Ng and Jamin Greenbaum all helped me to learn how to better quantify radar system performance, and all of them answered questions about the hardware.

References

- [1] CARTER, S. P., BLANKENSHIP, D. D., YOUNG, D. A., AND HOLT, J. W. Using radar-sounding data to identify the distribution and sources of subglacial water: application to Dome C, East Antarctica. *Journal of Glaciology* 55, 194 (2009), 1025–1040.
- [2] CASTELLETTI, D., SCHROEDER, D. M., HENSLEY, S., GRIMA, C., NG, G., YOUNG, D., GIM, Y., BRUZZONE, L., MOUSSESSIAN, A., AND BLANKENSHIP, D. D. Clutter Detection Using Two-Channel Radar Sounder Data.
- [3] FRETWELL, P., PRITCHARD, H. D., VAUGHAN, D. G., BAMBER, J. L., BARRAND, N. E., BELL, R., BIANCHI, C., BINGHAM, R. G., BLANKENSHIP, D. D., CASASSA, G., AND OTHERS. Bedmap2: improved ice bed, surface and thickness datasets for Antarctica. *The Cryosphere* 7, 1 (2013), 375–393.
- [4] GOGINENI, S., YAN, J. B., PADEN, J., LEUSCHEN, C., LI, J., RODRIGUEZ-MORALES, F., BRAATEN, D., PURDON, K., WANG, Z., LIU, W., AND OTHERS. Bed topography of Jakobshavn Isbræ, Greenland, and Byrd Glacier, Antarctica. *Journal of Glaciology* 60, 223 (2014), 813.
- [5] GREENBAUM, J. S., BLANKENSHIP, D. D., YOUNG, D. A., RICHTER, T. G., AITKEN, A. R. A., LEGRESY, B., SCHROEDER, D. M., ROBERTS, J. L., WARNER, R. C., VAN OMMEN, T. D., AND SIEGERT, M. J. Increased Ocean Access to Totten Glacier, East Antarctica. *Nature Geos* (2015).
- [6] GRIMA, C., KOFMAN, W., HERIQUE, A., OROSEI, R., AND SEU, R. Quantitative analysis of Mars surface radar reflectivity at 20MHz. *Icarus* 220, 1 (2012), 84–99.
- [7] GRIMA, C., SCHROEDER, D. M., BLANKENSHIP, D. D., AND YOUNG, D. A. Planetary landing-zone reconnaissance using ice-penetrating radar data: Concept validation in {Antarctica}. *Planetary and Space Science* (2014).
- [8] HOLSCUH, N., CHRISTIANSON, K., AND ANANDAKRISHNAN, S. Power loss in dipping internal reflectors, imaged using ice-penetrating radar. *Annals of Glaciology* 55, 67 (2014), 49.
- [9] MACGREGOR, J. A., FAHNESTOCK, M. A., CATANIA, G. A., PADEN, J. D., GOGINENI, S., YOUNG, S. K., RYBARIK, S. C., MABREY, A. N., WAGMAN, B. M., AND MORLIGHM, M. Radiostratigraphy and age structure of the Greenland Ice Sheet. *Journal of Geophysical Research: Earth Surface* (2015).
- [10] PETERS, M. E., BLANKENSHIP, D. D., CARTER, S. P., KEMPF, S. D., YOUNG, D. A., AND HOLT, J. W. Along-track focusing of airborne radar sounding data from West Antarctica for improving basal reflection analysis and layer detection. *Geoscience and Remote Sensing, IEEE Transactions on* 45, 9 (2007), 2725–2736.
- [11] PETERS, M. E., BLANKENSHIP, D. D., AND MORSE, D. L. Analysis techniques for coherent airborne radar sounding: Application to West Antarctic ice streams. *Journal of Geophysical Research: Solid Earth (1978–2012)* 110, B6 (2005).
- [12] SCHROEDER, D. M., BLANKENSHIP, D. D., RANEY, R. K., AND GRIMA, C. Estimating subglacial water geometry using radar bed echo specularity: Application to Thwaites Glacier, West Antarctica.

- [13] SCHROEDER, D. M., BLANKENSHIP, D. D., AND YOUNG, D. A. Evidence for a water system transition beneath Thwaites Glacier, West Antarctica. *Proceedings of the National Academy of Sciences* 110, 30 (2013), 12225–12228.
- [14] SCHROEDER, D. M., BLANKENSHIP, D. D., YOUNG, D. A., AND QUARTINI, E. Evidence for elevated and spatially variable geothermal flux beneath the West Antarctic Ice Sheet. *Proceedings of the National Academy of Sciences* 111, 25 (2014), 9070–9072.
- [15] SCHROEDER, D. M., BLANKENSHIP, D. D., YOUNG, D. A., WITUS, A. E., AND ANDERSON, J. B. Airborne radar sounding evidence for deformable sediments and outcropping bedrock beneath Thwaites Glacier, West Antarctica. *Geophysical Research Letters* (2014).
- [16] WU, X., JEZEK, K. C., RODRIGUEZ, E., GOGINENI, S., RODRIGUEZ-MORALES, F., AND FREEMAN, A. Ice sheet bed mapping with airborne SAR tomography. *Geoscience and Remote Sensing, IEEE Transactions on* 49, 10 (2011), 3791–3802.